

Renormalization of excitonic properties by polar phonons

Yoonjae Park¹ and David T. Limmer^{1, 2, 3, 4, a)}

¹⁾*Department of Chemistry, University of California, Berkeley*

²⁾*Materials Science Division, Lawrence Berkeley National Laboratory*

³⁾*Chemical Science Division, Lawrence Berkeley National Laboratory*

⁴⁾*Kavli Energy NanoScience Institute, Berkeley, California, Berkeley*

(Dated: 5 July 2022)

We employ quasiparticle path integral molecular dynamics to study how the excitonic properties of model semiconductors are altered by electron-phonon coupling. We describe ways within a path integral representation of the system to evaluate the renormalized mass, binding energy, and radiative recombination rate of excitons in the presence of a fluctuating lattice. To illustrate this approach, we consider Fröhlich-type electron-phonon interactions and employ an imaginary time influence functional to incorporate phonon-induced effects nonperturbatively. The effective mass and binding energies are compared with perturbative and variational approaches, which provide qualitatively consistent trends. We evaluate electron-hole recombination rates as mediated through both trap-assisted and bimolecular processes, developing a consistent statistical mechanical approach valid in the reaction limited regime. These calculations demonstrate how phonons screen electron-hole interactions, generically reducing exciton binding energies and increasing their radiative lifetimes.

I. INTRODUCTION

The application and design of photovoltaic devices rely on understanding the photophysics of semiconducting materials. Recent studies into novel low dimensional and hybrid perovskite semiconductors have highlighted the need to incorporate effects of a fluctuating lattice on the stationary behavior of excitons, moving away from the traditional perspectives in which screening is presumed to be largely determined by electronic degrees of freedom.^{1–7} While the study of electron-phonon coupling for free charges has a long history, including foundational studies on polarons,^{8–15} there is comparatively little known concerning the effects of electron-phonon coupling on excitonic properties. Motivated by observations that suggest polaronic effects play an important role in renormalizing exciton mobilities,¹⁶ binding energies, recombination rates^{17,18} and photoluminescence yields,¹⁹ we aim to fill this knowledge gap. In this work, we explore the effects of phonons on the excitonic properties of traditional and hybrid perovskite materials using a path integral approach. Working within a Fröhlich model Hamiltonian,⁸ we evaluate numerically exactly the role of phonons, finding that they generally reduce exciton binding energies and increase radiative lifetimes.

The static properties of excitons determine the power conversion efficiencies of photovoltaics, the quantum yields for light emission and more. Predicting these properties from molecular models is an area of active development.²⁰ Most widely used approaches build upon

ground state density functional theory, employing corrections from many-body physics including the GW approximation and Bethe-Salpeter equations.^{21–23} These and related approaches²⁴ have been successful for a wide range of semiconducting materials^{25,26} However, these theories traditionally ignore dynamical effects from phonons, as including them within this framework beyond is challenging. While historically, analytical approaches based on model Hamiltonians have been developed,^{27–29} recent efforts have focused on numerical methods to describe the effects of phonons approximately.^{30–33} While these approaches leverage powerful *ab initio* many body theories, they have been limited in the strength of the electron-phonon coupling that can be considered and the time and lengthscales approachable.

Here, we present a path integral approach for describing electron and hole quasiparticles interacting with phonons. Analogous quasiparticle path integral approaches have been utilized to describe photoinduced phase separation,^{34–36} charge trapping,^{37,38} and charge recombination,³⁹ as well as confinement effects.⁴⁰ We can derive an imaginary time influence functional, allowing us to incorporate dynamical and quantum mechanical effects of phonons within a harmonic approximation. To sample the resultant theory, we apply path integral molecular dynamics (MD) and study how electron-phonon coupling renormalizes the band mass, exciton binding energy, and electron-hole recombination rate for Fröhlich-type interactions between electron and hole quasiparticles and phonons. In the followings, we elaborate theoretical details of path integral approach applied to exciton with phonons, and present how to calculate each property within this framework followed by

^{a)}Electronic mail: dlimmer@berkeley.edu

the discussion on the effects of phonons.

II. THEORY

We consider a system composed of an electron and hole interacting with a field of phonons, whose effective Hamiltonian consists of three parts,

$$\hat{\mathcal{H}} = \hat{\mathcal{H}}_{\text{eh}} + \hat{\mathcal{H}}_{\text{ph}} + \hat{\mathcal{H}}_{\text{int}} \quad (1)$$

a part due to the electronic degrees of freedom, $\hat{\mathcal{H}}_{\text{eh}}$, a part from the lattice, $\hat{\mathcal{H}}_{\text{ph}}$, and their interaction, $\hat{\mathcal{H}}_{\text{int}}$. The electronic part includes the kinetic energies of an electron and a hole and a Coulomb interaction

$$\hat{\mathcal{H}}_{\text{eh}} = \frac{\hat{\mathbf{p}}_e^2}{2m_e} + \frac{\hat{\mathbf{p}}_h^2}{2m_h} - \frac{e^2}{4\pi\epsilon_r|\hat{\mathbf{x}}_e - \hat{\mathbf{x}}_h|} \quad (2)$$

where $\hat{\mathbf{p}}$ and $\hat{\mathbf{x}}$ are momentum and position operators of a quantum particle, ϵ_r is the dielectric constant in units of the vacuum permittivity ϵ_0 , and the subscript e and h indicate electron and hole. The masses m_e and m_h are taken as their corresponding band masses using an effective mass approximation. This simplification can be relaxed by parameterizing more elaborate kinetic energy functions with position dependent masses.⁴⁰

The lattice is described by a collection of harmonic modes

$$\hat{\mathcal{H}}_{\text{ph}} = \frac{1}{2} \sum_{\mathbf{k}} (\hat{\mathbf{p}}_{\mathbf{k}}^2 + \omega_{\mathbf{k}}^2 \hat{\mathbf{q}}_{\mathbf{k}}^2) \quad (3)$$

where $\hat{\mathbf{p}}_{\mathbf{k}}$ and $\hat{\mathbf{q}}_{\mathbf{k}}$ are the mass weighted momentum and coordinate of a phonon at wave vector \mathbf{k} . Without loss of generality, we will take the frequency of the oscillators to be constant $\omega_{\mathbf{k}} = \omega$, and equal to the longitudinal optical mode. While previous work has illustrated the importance of including additional modes or their wave-vector dependence in specific materials,^{33,39} we neglect these effects here in order to benchmark the approach to a simplified model. For generalizations, see App. A.

We adopt a Fröhlich-type interaction^{8,41} between the charges and the phonons, where a charged particle interacts linearly with the polarization field produced by a lattice vibration,

$$\hat{\mathcal{H}}_{\text{int}} = \sum_{\mathbf{k}} \hat{\mathbf{q}}_{\mathbf{k}} \frac{C_e e^{i\mathbf{k}\cdot\hat{\mathbf{x}}_e} - C_h e^{i\mathbf{k}\cdot\hat{\mathbf{x}}_h}}{\mathbf{k}} \quad (4)$$

where $\hat{\mathbf{q}}_{\mathbf{k}}$ corresponds to the polar displacement field that the charge can be coupled to along the \mathbf{k} direction. The strength of the coupling is set by a material specific constant

$$C_i = -i\hbar\omega \left(\frac{4\pi\alpha_i}{V} \right)^{\frac{1}{2}} \left(\frac{\hbar}{2m_i\omega} \right)^{\frac{1}{4}} \left(\frac{2\omega}{\hbar} \right)^{\frac{1}{2}} \quad (5)$$

where i indicates either electron or hole, V is the volume of the system, \hbar is Plank's constant divided by 2π and α is a dimensionless Fröhlich coupling constant.⁴¹ To study this system we employ a path integral formalism^{42,43} which allows us to describe the correlated behavior of the electron, hole, and phonons quantum mechanically and on an equal footing.⁴⁴ The partition function of the system can be written as

$$\mathcal{Z} = \int \mathcal{D}[\mathbf{x}_e, \mathbf{x}_h, \mathbf{q}_{\mathbf{k}}] e^{-\mathcal{S}[\mathbf{x}_e, \mathbf{x}_h, \mathbf{q}_{\mathbf{k}}]} \quad (6)$$

where the path action \mathcal{S} is defined as

$$\mathcal{S} = \frac{1}{\hbar} \int_{\tau=0}^{\beta\hbar} \mathcal{H}_{\text{eh},\tau} + \mathcal{H}_{\text{ph},\tau} + \mathcal{H}_{\text{int},\tau} \quad (7)$$

with the imaginary time variable τ , and $\beta^{-1} = k_{\text{B}}T$. The Hamiltonian indexed by τ represents the classical counterpart of Eqs. 2-4 at given τ where $\hat{\mathbf{p}}$ and $\hat{\mathbf{x}}$ are replaced by \mathbf{p}_{τ} and \mathbf{x}_{τ} for each quasiparticle.

Considering that the phonons act as a Gaussian field coupled linearly to the charge density, the phonon variables $\{\mathbf{q}_{\mathbf{k}}\}$ can be integrated out,^{39,42} yielding

$$\mathcal{Z} = \mathcal{Z}_{\text{ph}} \int \mathcal{D}[\mathbf{x}_e, \mathbf{x}_h] \exp \left[-\frac{1}{\hbar} \int_{\tau=0}^{\beta\hbar} \mathcal{H}_{\text{eh},\tau} + \mathcal{H}_{\text{eff},\tau} \right] \quad (8)$$

with \mathcal{Z}_{ph} the partition function of phonons without the charge. The resulting effective Hamiltonian at a given τ can be written as a sum of four pieces

$$\mathcal{H}_{\text{eff},\tau} = \sum_{i,j \in \{e,h\}} \mathcal{H}_{\text{eff},\tau}^{ij} \quad (9)$$

with

$$\mathcal{H}_{\text{eff},\tau}^{ij} = -\sigma_{ij} \frac{\alpha_{ij}\omega^2\sqrt{\hbar}}{\beta\sqrt{8m_{ij}\omega}} \int_{\tau'=0}^{\beta\hbar} \frac{e^{-\omega|\tau-\tau'|}}{|\mathbf{x}_{i,\tau} - \mathbf{x}_{j,\tau'}|} \quad (10)$$

where $\alpha_{ij} = \sqrt{\alpha_i\alpha_j}$, $m_{ij} = \sqrt{m_i m_j}$, and σ_{ij} is $+1/-1$ for the same/opposite charges. We have used the inverse Fourier representation of \mathbf{k}^{-2} with the equation for $C_{i/j}$ given in Eq. 5. In order to use these results computationally, we discretized the imaginary time interval into n slices. In this discrete formulation, the effective Hamiltonian $\mathcal{H} = \mathcal{H}_{\text{eh}} + \mathcal{H}_{\text{eff}}$ becomes

$$\mathcal{H}_{\text{eh}} = \sum_{i,t} \frac{m_i n}{2\beta^2 \hbar^2} (\mathbf{x}_{i,t} - \mathbf{x}_{i,t+1})^2 - \sum_t \frac{e^2}{4\pi\epsilon_r n |\mathbf{x}_{e,t} - \mathbf{x}_{h,t}|} \quad (11)$$

where we denote the last sum \mathcal{H}_{C} and

$$\mathcal{H}_{\text{eff}} = \sum_{i,j} \mathcal{H}_{\text{eff}}^{ij} = - \sum_{i,j} \sum_{t,s} \sigma_{ij} \frac{\alpha_{ij}\beta\hbar^{5/2}\omega^2}{n^2\sqrt{8m_{ij}\omega}} \frac{e^{-\frac{\beta\hbar\omega}{n}|t-s|}}{|\mathbf{x}_{i,t} - \mathbf{x}_{j,s}|} \quad (12)$$

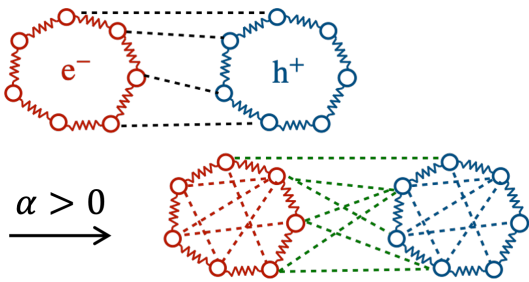


FIG. 1. Illustration of imaginary time paths without (top) and with (bottom) phonon effects where black dotted lines represent a bare Coulomb attraction, red and blue dotted lines describe the induced attractive self-interaction for the electron and hole, respectively, and the green dotted lines represent the effective screened interaction due to the dynamic phonons.

where $i, j \in \{e, h\}$ and $t, s \in [1, n]$. The number of timeslices, or beads, is a convergence parameter that needs to be taken large for accuracy.⁴⁵

In the path integral framework, Eq. 11 implies that electron and hole quasiparticles are represented as classical ring polymers⁴⁶ consisting of n identical beads, where adjacent beads are harmonically coupled and beads with the same index from electron and hole are interacting through a fraction of Coulomb potential. Additionally from Eq. 12, the effective energy induced by phonons depends on the positions of two different imaginary times, represented as the interaction between beads, and the stiffness of phonons sets the decaying imaginary timescale. In this way, we employ an imaginary time influence functional formalism which is shown schematically shown in Fig. 1. Two effects from the phonons are clear from this picture. First, individual charges are localized by the phonons due to the induced attractive self-interaction. Second, the electron-hole interaction is weakened due to the induced repulsion, which is a reflection of phonon screening. The implications of these two effects are explored below.

III. SIMULATION DETAILS

To study the utility and efficiency of this approach, we consider models motivated by CdS and MAPbI₃, whose material properties are in different regimes of band mass and electron-phonon coupling strength. CdS is a traditional II-IV semiconductor where the material specific Fröhlich coupling constant α is small, 0.53, and the band mass of the hole is much heavier than the mass of electron. For MAPbI₃, a lead-halide perovskite, the electron and hole have nearly the same band mass and the coupling strength is intermediate $\alpha = 1.72$. For the pur-

pose of this paper, since we aim to use the path integral method to study the general effects of electron-phonon coupling, we will ignore the anharmonic corrections from the lattice which can be important in determining the optoelectronic properties of these materials.^{6,17–19,39} Parameters used in simulations are summarized in Table 1.

For both materials, we use MD simulations to sample the effective actions with fictitious masses for the beads kept at 1 amu, and we study the renormalization of the effective mass, exciton binding energy, and recombination rate due to electron-phonon coupling. For the effective mass calculations, $\mathcal{H}_{\text{eff}}^{ee}$ defined in Eq. 12 is used as the system Hamiltonian and for the other two properties, we run simulations of an electron-hole pair described as two ring polymers where one has a unit negative charge for an electron and the other has a unit positive charge for a hole with the Hamiltonian $\mathcal{H} = \mathcal{H}_{\text{eh}} + \mathcal{H}_{\text{eff}}$ given in Eq. 11 and Eq. 12.

To avoid the divergence in the $1/|\mathbf{x}|$ term between attractive beads, a pseudopotential is used where $1/|\mathbf{x}|$ is replaced by $(r_c^2 + \mathbf{x}^2)^{-1/2}$ and r_c is chosen to reproduce the band gap of each material.⁵² Simulations are run in an ensemble with constant volume, particle number and temperature using a Langevin thermostat where the total momentum averages to zero with integration time step 1.0 fs and at room temperature unless explicitly specified, using the LAMMPS⁵³ package. For the following sections, we present a way to compute each property within the path integral framework followed by the discussion on the effects from phonons where α serves as a control parameter for the interaction strength between charges and phonons.

Parameter (unit)	CdS	MAPbI ₃
electron band mass m_e (m_0)	0.19 ⁴⁷	0.20 ⁴⁸
hole band mass m_h (m_0)	0.80 ⁴⁷	0.20 ⁴⁸
optical frequency ω (THz)	9.14 ⁴⁹	7.53 ⁵⁰
dielectric constant ϵ_r (ϵ_0)	5.7 ⁴⁷	6.1 ⁴⁸
band gap E_{gap} (eV)	2.58 ⁴⁷	1.64 ⁵¹
Fröhlich constant α_e (-)	0.53 ¹⁵	1.72 ⁵⁰

TABLE 1. Simulation parameters for CdS and MAPbI₃ where m_0 is a bare mass of electron, ϵ_0 is the vacuum permittivity, and the Fröhlich constant for a hole can be calculated by $\alpha_h = \alpha_e \sqrt{m_h/m_e}$.

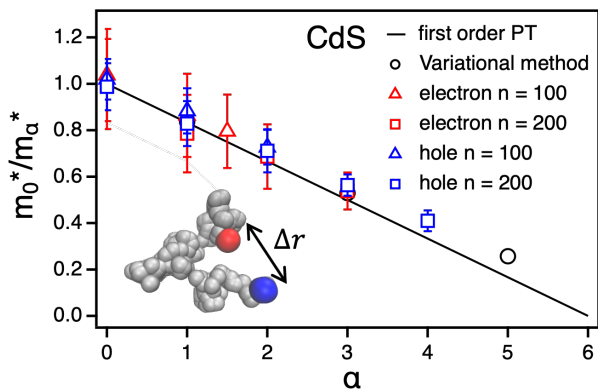


FIG. 2. Inverse effective mass with phonons m_α^* relative to the band mass m_0^* as a function of coupling strength α . Red/blue symbols represent the results for an electron/hole quasiparticles with different number of beads n . Black solid line and circles are the results predicted from first order perturbation theory and Feynman's variational approach.⁵⁴ Inset figure is simulation snapshot for the schematic of Δr where red and blue represent the first and the last beads.

IV. EFFECTIVE MASS

To validate the path integral framework, we first study the effective mass, for which significant previous analysis has been undertaken.^{43,55} Since the presence of a charge induces a distortion to the lattice, motion of the charge requires moving the corresponding distortion field, renormalizes the mass of the charge, making it heavier. Within the path integral framework, since the effective mass is a momentum-dependent quantity, an inverse effective mass can be computed with an open-chain ring polymer in the low temperature limit as^{55,56}

$$\frac{1}{m^*} = \lim_{\beta \rightarrow \infty} \frac{\langle (\Delta r)^2 \rangle}{3\beta\hbar^2} \quad (13)$$

where $\langle \dots \rangle$ denotes ensemble average and Δr is the distance between the first and the last beads, schematically shown in Fig. 2 inset.

For simplicity, a Feynman unit system where $k_B = \hbar = \omega = m = 1$ is used in this calculation. Given that Eq. 13 is valid at low temperature, we tune the temperature and pseudopotential parameters and set $k_B T / \hbar \omega = 0.02$ and $r_c = 0.0707$ which are low and small enough for the convergence of our results. Figure. 2 describes the inverse effective mass of electron and hole quasiparticles of CdS at different α where each point is the value averaged over 20 ensembles from simulations performed in constant volume, particle number, and temperature. We find that the lighter mass and the stronger coupling require larger number of beads to converge. The results from path integral approach are consistent with the value predicted

from first order perturbation theory for small α ,¹⁵

$$\frac{m_0^*}{m_\alpha^*} = 1 - \frac{\alpha}{6} \quad (14)$$

shown in Fig. 2. The calculations are consistent with Feynman's variational approach⁵⁴ which is known as the most accurate solution across α , demonstrating the validity of this framework and the n required for convergence at various α .

V. EXCITON BINDING ENERGY

Within the path integral framework, we capture the full correlation energy between the electron and hole quasiparticles, allowing us to compute accurate exciton binding energies. Here we show how electron-phonon coupling alters the binding energy. We compute the exciton binding energy from the average energy of exciton⁵⁷

$$\langle E \rangle = -\frac{\partial}{\partial \beta} \ln \int \mathcal{D}[\mathbf{x}_e, \mathbf{x}_h] e^{-\beta \mathcal{H}} \quad (15)$$

resulting in two pieces, the average kinetic energy $\langle E \rangle_K$ and the average potential energy $\langle E \rangle_P$. For the kinetic energy, since the relevant terms produced by Eq. 15 diverge as $n \rightarrow \infty$, we use a virial estimator,⁴⁵ which is known as an efficient way to estimate the kinetic energy in path integral simulations to avoid the large fluctuations from the subtraction of two diverging terms. Using the derivative of potential energy, the average kinetic energy can be written as

$$\begin{aligned} \langle E \rangle_K = & 3k_B T + \frac{1}{2} \sum_{i \in \{e, h\}} \sum_{t=1}^n \left\langle \mathbf{x}_{i,t} \cdot \frac{\partial (\mathcal{H}_C + 2\mathcal{H}_{\text{eff}}^{eh})}{\partial \mathbf{x}_{i,t}} \right\rangle \\ & + \frac{1}{2} \sum_{t=1}^n \left\langle \mathbf{x}_{e,t} \cdot \frac{\partial \mathcal{H}_{\text{eff}}^{ee}}{\partial \mathbf{x}_{e,t}} \right\rangle + \frac{1}{2} \sum_{t=1}^n \left\langle \mathbf{x}_{h,t} \cdot \frac{\partial \mathcal{H}_{\text{eff}}^{hh}}{\partial \mathbf{x}_{h,t}} \right\rangle \end{aligned} \quad (16)$$

and the average potential energy becomes

$$\langle E \rangle_P = \langle \mathcal{H}_C \rangle + \sum_{i, j \in \{e, h\}} 2\langle \mathcal{H}_{\text{eff}}^{ij} \rangle - \langle \mathcal{H}_{\text{eff}}^{ij} \rangle' \quad (17)$$

where $\langle \mathcal{H}_{\text{eff}}^{ij} \rangle'$ is defined as $\langle \mathcal{H}_{\text{eff}}^{ij} \rangle$ given by Eq. 12 with an additional factor of $\beta \hbar \omega |t - s| / n$ inside the summations with respect to t and s .

The exciton binding energy is the energy threshold for an optical absorption between conduction and valence bands and thus traditionally reported in the low temperature limit. To evaluate it, we compute the average energy difference between the exciton and separately the electron and hole, at different temperatures and extrapolate to zero temperature, $E_B = \lim_{T \rightarrow 0} \langle E \rangle_{\text{ex}} - \langle E \rangle_e - \langle E \rangle_h$.

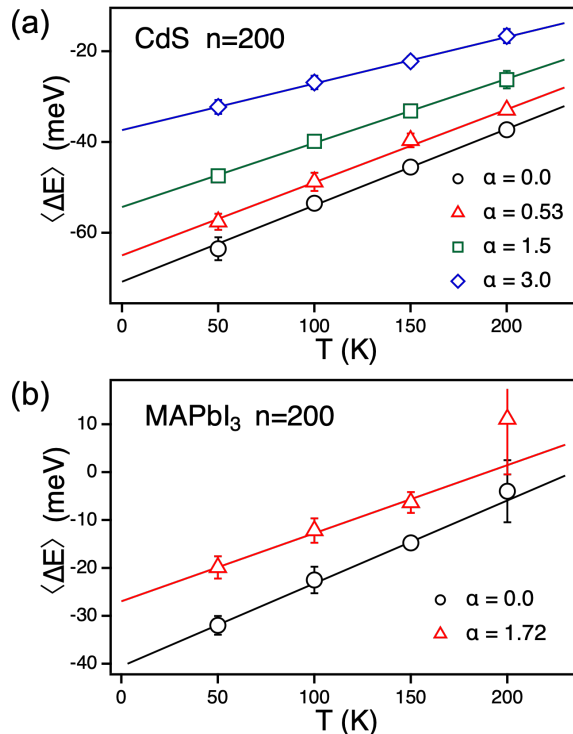


FIG. 3. Average energy difference computed from path integral simulations at different temperatures and coupling strength α for (a) CdS and (b) MAPbI₃ with 200 beads. Solid lines are linearly fitted lines.

The subscript ex denotes an average with both electron and hole, while e/h refers to calculations of the self energies of the electron/hole where the of quasiparticles interacts only with surrounding phonons.

Figures 3 (a) and (b) show the average energy difference at different temperatures for CdS and MAPbI₃. In both cases, we consider $\alpha = 0$ and compare to $\alpha > 0$, and find that $n = 200$ is large enough to converge the result. The extrapolated exciton binding energies are summarized in Table 2. We find that exciton energy becomes lower at high temperature, reflective of the higher population of phonons to stabilize the free charges. Also, as the electron-phonon interaction becomes stronger, the exciton binding energy becomes smaller, implying that the phonons screen the effective electron-hole interaction.

For the results without phonons, $\alpha = 0$, we compare our path integral simulations with binding energies from the Wannier-Mott exciton⁵⁸ which is equivalent to our system.⁵⁹ The exciton binding energy is computable exactly and given by $E_B^H = \mu e^4 / 2(4\pi\epsilon_r)^2 \hbar^2$ with $\mu = m_e m_h / (m_e + m_h)$ as the reduced mass of exciton. Calculated hydrogenic binding energies are 64.3 meV and 36.6 meV for CdS and MAPbI₃, consistent within a few meV with our values in both materials, showing the robustness

CdS α	0.0	0.53	1.5	3.0
E_B (meV)	70.8	65.0	54.3	37.4
MAPbI ₃ α	0.0	1.72	-	-
E_B (meV)	40.6	27.0	-	-

TABLE 2. Calculated exciton binding energy E_B for CdS and MAPbI₃ under different coupling strength.

of the calculation with the path integral framework. In the presence of electron-phonon interaction with nonzero value of α , we compare the binding energies from the corresponding coupling strength, $\alpha = 0.53$ for CdS and $\alpha = 1.72$ for MAPbI₃, with the prediction from perturbation theory and Pollmann-Buttner theory.²⁸ The approximated differences in binding energies from the first order perturbation theory, $\Delta E_B^F = E_{B,\alpha=0} - E_{B,\alpha \neq 0} \approx -2\alpha \hbar \omega$, are 6.4 meV and 17.1 meV for CdS and MAPbI₃, which are higher than our results, 5.8 meV for CdS and 13.6 meV for MAPbI₃. Pollmann-Buttner theory results from a canonical transformation of the original Hamiltonian, which in the weak electron-phonon coupling limit provides an effective potential between the electron and hole. Binding energies estimated by solving Schrodinger equation using Pollmann-Buttner potential between the electron and hole in App. B are 41.3 meV and 16.7 meV for CdS and MAPbI₃, lower than results from the path integral simulations. We suspect the differences are attributed to the neglect of charge density relaxation due to hybridization with the phonons in perturbation theory and Pollmann-Buttner theory. This is likely a larger effect in MAPI₃ because of the equal masses of the electron and hole renders phonon screening at short distances a higher order process. Considering the fact that the anharmonicity from the lattice is not taken into account, the path integral estimates of the binding energies are in reasonable agreement with typical experimental values, of 28 meV⁶⁰ and 16 meV⁶¹ for CdS and MAPI₃.

VI. ELECTRON-HOLE RECOMBINATION RATE

We now investigate the electron-hole recombination rate, which typically dominates the lifetime of charge carriers in bulk semiconducting materials.²⁰ It has been generally accepted that charge carrier recombination can be divided into three different mechanisms.^{17,61} The first is trap-assisted recombination where one charge carrier is trapped by a defect or impurity and then recombination occurs from the trap state. The second is due to bimolecular recombination where an electron in the conduction

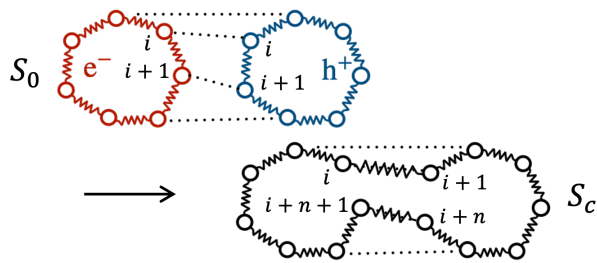


FIG. 4. Schematics of \mathcal{S}_0 and \mathcal{S}_c where two separate paths (top) are combined at some imaginary time i to form a combined radiating path (bottom).

band is combined with a hole in the valence band, which is a predominant radiative pathway for direct semiconductors under standard operating conditions.⁶² Finally, Auger recombination in which electron and hole are recombined through an energy transfer to other charge carriers or phonons is yet a higher order process. While Auger recombination can be important in nanocrystals, it is typically negligible in bulk materials.^{63,64}

All the mechanisms described above contribute to the recombination process but depending on the concentration of charge carriers, the dominant pathway varies. At low density, trap assisted recombination will dominate and at high density, Auger recombination will matter. In this work, we assume that the contribution from Auger recombination is small and consider the first and second order recombination processes. For a charge neutral system the electron and hole concentrations are equal $\rho_e = \rho_h$, and the rate equation is given by

$$\frac{d\rho_e}{dt} = -k_m\rho_e - k_b\rho_e^2 = -k_{\text{tot}}\rho_e \quad (18)$$

where $k_{m/b}$ is the rate constant for trap-assisted/bimolecular recombination process with k_{tot} as the overall rate constant.

Independent of the mechanism, the radiative recombination rate of an electron-hole pair within the path integral framework is given by⁶⁵

$$k_r = \frac{e^2\sqrt{\epsilon_r}E_{\text{gap}}^2}{2\pi\epsilon_0\hbar^2c^3\mu} \frac{\mathcal{Z}_c}{\mathcal{Z}_0} \quad (19)$$

originating from Fermi's golden rule for spontaneous emission under our effective mass approximation, where c is the speed of light and E_{gap} is the band gap energy. Other parameters for CdS and MAPbI₃ are summarized in Table 1.

The rate in Eq. 19 is proportional to a ratio of partition functions whose subscripts 0 and c indicate the standard thermal trace and the trace for a *radiating path* where two separate imaginary time paths for quasiparticles are combined at a common imaginary time schematically shown

in Fig. 4. This ratio is identical to a thermally averaged overlap integral between the electron and hole densities. The partition functions are related through

$$\mathcal{Z}_c = \mathcal{Z}_0 \int \mathcal{D}[\mathbf{x}_e, \mathbf{x}_h] \frac{e^{-S_0}}{\mathcal{Z}_0} e^{-S_c+S_0} = \mathcal{Z}_0 \langle e^{\Delta S} \rangle_0 \quad (20)$$

where ΔS is the change in path action. It is convenient for sampling purposes to rewrite this average using a conditional probability representation,

$$P(\Delta S) = \int d\mathbf{R} P(\Delta S|\mathbf{R})P(\mathbf{R}) \quad (21)$$

so that the ratio in the dilute limit can be written as

$$\frac{\mathcal{Z}_c}{\mathcal{Z}_0} = \rho_e \int d\mathbf{R} \langle e^{\Delta S} \rangle_{\mathbf{R}} e^{-\beta\Delta F(\mathbf{R})} \quad (22)$$

where \mathbf{R} is the vector between electron and hole ring polymers, represented by $\beta F(R) = -\ln P(R)$ a free energy for changing their distance. The difference in path actions is equal to

$$\begin{aligned} \Delta S = & \sum_{t=1}^n \frac{m_e n}{2\beta\hbar^2} (\mathbf{x}_{e,t} - \mathbf{x}_{e,t+1})^2 + \frac{m_h n}{2\beta\hbar^2} (\mathbf{x}_{h,t} - \mathbf{x}_{h,t+1})^2 \\ & - \sum_{t=1}^{2n} \frac{\mu n}{\beta\hbar^2} (\mathbf{x}_{c,t} - \mathbf{x}_{c,t+1})^2 \end{aligned} \quad (23)$$

for going between the thermal and radiating paths. The first two terms correspond to \mathcal{S}_0 , and \mathcal{S}_c is given by the last term, and the index of beads for the combined coordinates $\{\mathbf{x}_c\}$ is schematically described in Fig. 4. In the following, we present the details on simulations and discussions on trap-assisted and bimolecular recombination rates, and combine these two to estimate a total rate constant. In both, we assume that recombination is not limited by diffusion of the charge carriers, so that a local equilibrium distribution is established for the relative positions of electrons and holes. For both, we will evaluate the rate at room temperature $T = 298K$.

A. Trap assisted recombination rate

For trap-assisted recombination, we need to describe the trapping of a charge as well as the subsequent recombination of electron and hole quasiparticles. To describe this process we assume that the trapped charge achieves a steady state population, and the rate is given by the likelihood of finding a trapped charge times the rate to recombine that trapped charge with an incoming charge,

$$k_m = P_{\text{trap}}k_r \quad (24)$$

where P_{trap} is the probability of an electron to be trapped. This approximation is valid in the dilute limit, provided trapping is reversible. For both CdS and MAPbI₃, we consider the trapping of an electron with a positively charged point defect. The point defect is described by a Coulomb potential acting between the defect and charge, determined by the corresponding dielectric constant ϵ_r and r_c which is set to recover the reported trapping energy, 1.75⁶⁷(0.3⁶⁸) eV for CdS (MAPbI₃).

In equilibrium, the probability of finding an electron trapped by an isotropic point defect is given by

$$P_{\text{trap}} = 4\pi\rho_d \int_0^{R_d^*} dR_d R_d^2 e^{-\beta\Delta F_d(R_d)} \quad (25)$$

where ρ_d is the density of defect sites in the lattice where it is possible to trap an electron, R_d^* is a cut-off distance for defining the trapped state, and $F_d(R_d)$ is the potential of mean force between the point defect and the electron, assuming both are dilute. To evaluate P_{trap} , we employ umbrella sampling⁶⁹ and Weighted Histogram Analysis Method^{70,71} by adding a bias potential $V(R_d) = 0.5k_{\text{sp}}(R_d - R_{\text{eq}})^2$ on the distance between the defect and the centroid of the electron ring polymer with $k_{\text{sp}} = 0.2 \text{ kcal/mol/\AA}^2$ and $\{R_{\text{eq}}\} = \{3\text{\AA}, 6\text{\AA}, \dots, 195\text{\AA}\}$. This allows us to determine the potential of mean force,

$$\beta F_d(R_d) = -\ln\langle\delta(R_d - |\mathbf{x}_d - \mathbf{x}_e^c|)\rangle \quad (26)$$

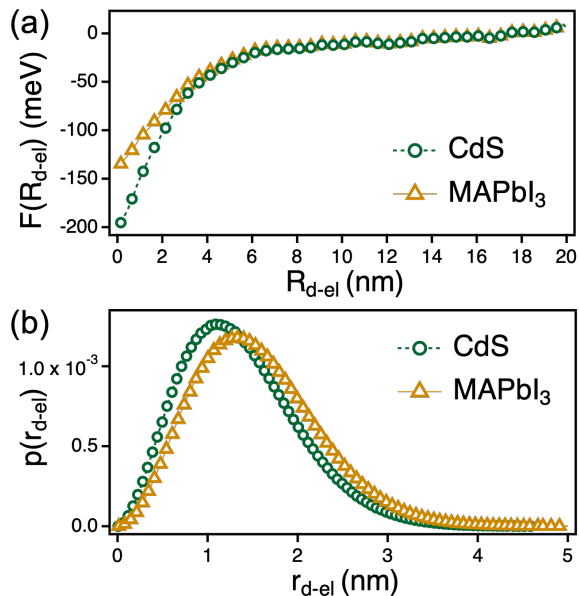


FIG. 5. (a) Free energy as a function of the distance between a defect and electron from 1 ring polymer simulation for CdS (green) and MAPbI₃ (orange). (b) Charge distribution for an electron localized on a defect for CdS (green) and MAPbI₃ (orange). Lines are guides to the eye.

with R_d as the distance between the defect \mathbf{x}_d and the centroid of the electron ring polymer \mathbf{x}_e^c .

The potential of mean force between an electron and the defect is shown in Fig. 5 a). For both CdS and MAPbI₃, the potential is monotonic. The binding free energy of the electron to the defect is much less than the bare potential energy of the pseudo-potential, reflecting the charge delocalization. This delocalization is evident in Fig. 5 b) which describes the charge distribution of the electron as a function of the distance between a point defect, $r_{d-el} = |\mathbf{x}_d - \mathbf{x}_e^c|$. For a free electron at large distance, the electron has a spatial extent defined by the radius of gyration of the imaginary time slices which is related to the thermal wavelength λ at given temperature and mass, $R_g(\beta, m) = \hbar\sqrt{\beta}/2\sqrt{m}$. For CdS and MAPbI₃ these free particle sizes are both nearly 20 Å. Upon trapping to a defect, the electrons of both CdS and MAPbI₃ become slightly more localized, with characteristic sizes of 15 Å and 17 Å respectively.

Given an equilibrium concentration of trapped electrons, the recombination rate is then evaluated by computing the likelihood of finding a hole in the vicinity of the electron and then measuring the conditional overlap in their densities, as described in Eq. 19. To evaluate both, we run MD simulations with a hole ring polymer as well as an electron ring polymer trapped into the point defect where Eq. 11 and 12 are used for two ring polymers. To sample the trajectory efficiently, we add the same harmonic potentials described above along the distance between two centroids of ring polymers and additional harmonic potentials with $k_{\text{sp}} = 0.5 \text{ kcal/mol/\AA}^2$ and $R_{\text{eq}} = 0.0$ on the distance between point defect and the centroid of electron ring polymer to hold an electron near the defect. This potential is unweighted analogously with WHAM to yield an unbiased distribution.

The resultant trap-assisted rate constants under different electron-phonon coupling strengths with $\rho_d = 10^{18} \text{ cm}^{-3}$ are summarized in Table 3. We find that the interaction with phonons reduces the rate constant in both materials although values with finite coupling strength in CdS are not significantly distinct. This reduction results from the smaller likelihood of finding a hole in the vicinity of the electron, a manifestation of dynamical screening from the phonons. This is explored more directly for bimolecular recombination below.

B. Bimolecular recombination rate

Bimolecular recombination is studied through the same method described above with MD simulations of electron and hole ring polymers. The bimolecular recombination

CdS α	0.0	0.53	1.5	3.0
k_m (μs^{-1})	0.93	0.37	0.36	0.44
$k_b\rho_e$ (ns^{-1})	0.101	0.082	0.032	0.025
τ_{tot} (ns)	9.79	12.2	31.3	39.6
MAPbI ₃ α	0.0	1.72	-	-
k_m (μs^{-1})	0.115	0.073	-	-
$k_b\rho_e$ (ns^{-1})	0.067	0.028	-	-
τ_{tot} (ns)	15.0	35.5	-	-

TABLE 3. Calculated trap-assisted rate k_m and bimolecular recombination rate constant k_b with the defect density $\rho_d = 10^{18}\text{cm}^{-3}$ and the carrier density $\rho_e = 10^{17}\text{cm}^{-3}$, and carrier lifetime τ_{tot} from k_{tot} for CdS and MAPbI₃ under different coupling strength. The mean statistical errorbar in these estimates is 10%.

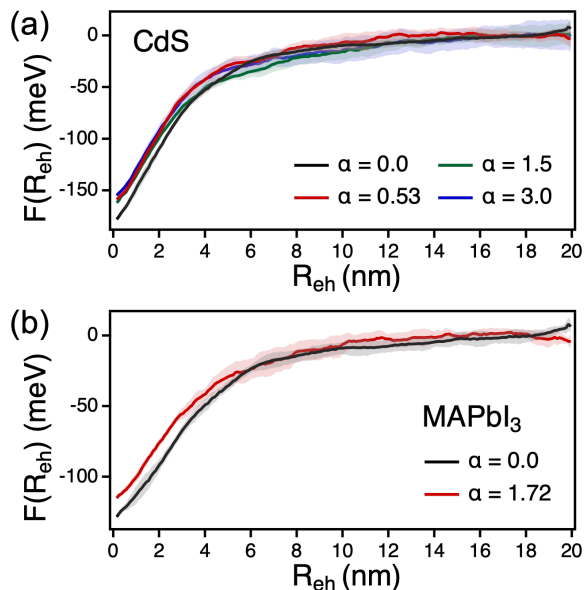


FIG. 6. Potentials of mean force for the charge centers. Potentials of mean force for (a) CdS and (b) MAPbI₃ for a variety of electron-phonon coupling strength α . Error bars are shown as shaded regions.

rate, $k_b\rho_e = k_r$, requires us to evaluate the potential of mean force for localizing the two charges and their subsequent overlap density. The potential of mean force, $F(R_{eh})$, between the centroids of electron \mathbf{x}_e^c and hole \mathbf{x}_h^c ring polymers,

$$\beta F(R_{eh}) = -\ln\langle\delta(R_{eh} - |\mathbf{x}_e^c - \mathbf{x}_h^c|)\rangle \quad (27)$$

is computable from umbrella sampling using the same procedure as that for the R_d . The resulting function is

shown in Fig. 6 for both CdS and MAPbI₃ as functions of electron-phonon coupling, α . The monotonic free energies display systematic destabilization of the electron-hole pair with increasing α , consistent with the reduction in exciton binding energies. Similarly, the minimum is more shallow for MAPbI₃ than for CdS.

In addition to the decreased likelihood of finding electron and hole pairs together, with increasing α the charge density distribution is broadened. Shown in Fig. 7 are the probability distributions of the distance between electron and hole beads, $r_{eh} = |\mathbf{x}_e - \mathbf{x}_h|$, at each strength of interaction with phonons. In both materials, the stronger the phonon interaction is, the larger the average bead-bead distance becomes, implying that phonons make an effective electron-hole interaction weaker through screening. The comparison between results from path integral simulation with the probability distribution predicted from Wannier-Mott exciton using hydrogen model shown in purple lines in Fig. 7 implies the importance of capturing the fluctuations of quasiparticles at room temperature.

The ratio of path partition functions $\mathcal{Z}_c/\mathcal{Z}_0$ for the bimolecular rate constant can be computed and extrapolated to the large n limit in order to extract a converged overlap element, as shown in App. C. The calculated bimolecular recombination rates for both materials with typical charge density $\rho_e = 10^{17}\text{cm}^{-3}$ are summarized in Table 3 as a function of α . The rates are found for both materials to decrease significantly over the range of electron-phonon coupling strength considered. MAPbI₃ is found to have a longer charge carrier lifetime than the CdS, which is due to enhanced screening of the former.

C. Total recombination rate

Combining trap-assisted and bimolecular rates, the total recombination rates defined in Eq. 18 are summarized in Table 3 with a typical charge carrier density $\rho_e = 10^{17}\text{cm}^{-3}$ and the defect density $\rho_d = 10^{18}\text{cm}^{-3}$ for both materials. We find that the radiative recombination is predominantly determined by bimolecular process. In both materials, electron-phonon coupling generally decreases recombination rate, resulting in the increase in the lifetime of charge carriers. The value obtained for CdS is in very good agreement with that observed from photoluminescence lifetime measurements on large spherical nanocrystals, 13 ns, but underestimates the lifetime reported for MAPbI₃ by a factor of 2, 70-100 ns.⁶¹ The latter disagreement can be attributed to the neglect of anharmonic effects accounted by the \mathbf{k} -dependence of correlation function in the optical mode which can be considered previously³⁹ and results in an effective electron-

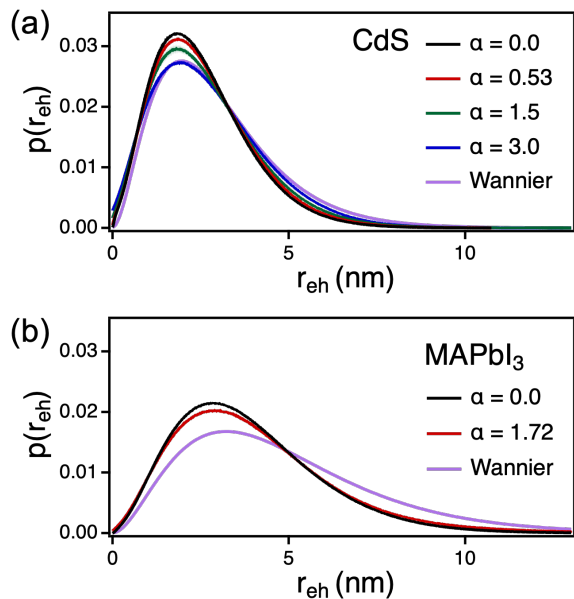


FIG. 7. Electron-hole charge density distributions. Charge density distributions for (a) CdS and (b) MAPbI₃ for a variety of electron-phonon coupling strength α evaluated at $T = 50$ K, compared to the Wannier model. Error bars are shown as shaded regions.

hole repulsion that has not been considered here.

VII. CONCLUSIONS

In summary, we have shown how a path integral approach can be used to study excitonic properties in the presence of dynamical phonons. We have presented ways to compute the renormalization of the binding energy and recombination rate, and validated these results in limiting regimes. While we have considered a simple model for an exciton in a polar lattice as being coupled through a Fröhlich interaction with a single optical mode, the influence functional approach employed is general and can easily be extended to many modes, arbitrary linear coupling forms, and in principle parameterized through *ab initio* methods. Additionally, while we have considered phonon effects on a single exciton in this work, this can be applied to multiple excitons and further combined with confining potentials.

ACKNOWLEDGMENTS

This work was supported by the U.S. Department of Energy, Office of Science, Office of Basic Energy Sciences, Materials Sciences and Engineering Division under

Contract No. DEAC02-05-CH11231 within the Physical Chemistry of Inorganic Nanostructures Program (No. KC3103). This research used resources of the National Energy Research Scientific Computing Center (NERSC), a U.S. Department of Energy Office of Science User Facility. Y.P. acknowledges the Kwanjeong Educational Foundation. D.T.L. acknowledges the Alfred P. Sloan Foundation.

Appendix A: Generalized influence functional

In the main text we have focused on a simplified model whereby the electron and hole are coupled to a single optical phonon through a linear Fröhlich coupling. For more complex lattice models where multiple dispersive modes are relevant, the influence functional formalism employed can be generalized. For many modes, the classical Hamiltonian entering into the path action can be written as

$$\mathcal{H}_{\text{ph}} = \frac{1}{2\beta\hbar} \int_{\tau=0}^{\beta\hbar} \sum_{\mathbf{k}} (\dot{\mathbf{q}}_{\mathbf{k},\tau}^2 + \omega_{\mathbf{k}}^2 \mathbf{q}_{\mathbf{k},\tau}^2) \quad (\text{A1})$$

where $\mathbf{q}_{\mathbf{k},\tau}$ is the classical displacement of the \mathbf{k} mode at imaginary time τ , and $\omega_{\mathbf{k}}$ is its corresponding frequency. For a generalized linear coupling between the charge density and the lattice of the form

$$\mathcal{H}_{\text{int}} = \frac{1}{\beta\hbar} \int_{\tau=0}^{\beta\hbar} \sum_{\mathbf{k}} \mathbf{q}_{\mathbf{k},\tau} \frac{C_{e,\mathbf{k}} e^{i\mathbf{k}\cdot\mathbf{x}_{e,\tau}} - C_{h,\mathbf{k}} e^{i\mathbf{k}\cdot\mathbf{x}_{h,\tau}}}{\mathbf{k}} \quad (\text{A2})$$

where $C_{e/h,\mathbf{k}}$ are generalized coupling coefficients, the phonons can still be integrated out. This yields an effective potential between the electron and hole of the form

$$\mathcal{H}_{\text{eff},\tau}^{ij} = -\frac{\sigma_{ij}}{2\beta\hbar} \sum_{\mathbf{k}} \int_{\tau'=0}^{\beta\hbar} C_{i,\mathbf{k}} C_{j,\mathbf{k}}^* \frac{e^{-i\mathbf{k}\cdot|\mathbf{x}_{i,\tau} - \mathbf{x}_{j,\tau'}|}}{k^2} \chi_{\mathbf{k}}(\tau - \tau') \quad (\text{A3})$$

where $\chi_{\mathbf{k}}(\tau - \tau') = \langle \mathbf{q}_{\mathbf{k}}(0) \mathbf{q}_{\mathbf{k}}(\tau - \tau') \rangle$ is the imaginary time correlation function of mode $\mathbf{q}_{\mathbf{k}}$. In Fourier space, the correlation function is given by

$$\chi_{\mathbf{k}}(\omega) = \frac{1}{\omega^2 + \omega_{\mathbf{k}}^2} \quad (\text{A4})$$

a sum of poles. In the classical limit, $\beta\hbar\omega_{\mathbf{k}} \rightarrow 0$, this influence functional returns a Coulomb potential screened by a wavevector dependent dielectric susceptibility.³⁹

Appendix B: Pollmann-Buttner theory

In order to compare our exciton binding energies to Pollmann-Buttner theory,²⁸ we parameterize an effective

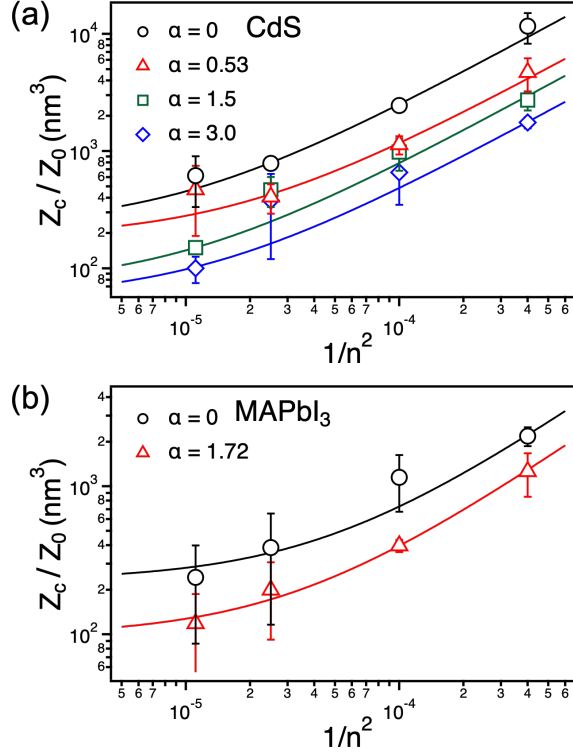


FIG. 8. Relative path partition functions for the radiative rate calculation. Convergence of the overlap for (a) CdS and (b) MAPbI₃. The values of α considered are $\{0, 0.53, 1.5, 3\}$ for CdS and $\{0, 1.72\}$ for MAPbI₃. Solid lines have the form $a + b/n^2$ where a and b are positive constants.

potential of the form

$$V_{\text{eff}}(r) = -\frac{e^2}{4\pi\epsilon_s r} - \frac{e^2}{4\pi\epsilon^* \Delta m r} \left(m_h e^{-r/R_h} - m_e e^{r/R_e} \right) \quad (\text{B1})$$

where $\Delta m = m_h - m_e$, $1/\epsilon^* = 1/\epsilon_r - 1/\epsilon_s$, $R_{e/h} = \sqrt{\hbar/2m_{e/h}\omega}$ with a static dielectric constant ϵ_s , which is taken to be 8.9 and 24.1 for CdS and MAPbI₃. We solve the time independent Schrodinger equation using this potential in the relative coordinate system for the electron and hole, \mathbf{r}_{eh} . This takes the form

$$-\frac{\hbar^2}{2\mu} \nabla^2 \phi_n(\mathbf{r}_{eh}) + V_{\text{eff}}(r_{eh}) \phi_n(\mathbf{r}_{eh}) = E_n \phi_n(\mathbf{r}_{eh}) \quad (\text{B2})$$

where E_n and $\phi_n(\mathbf{r}_{eh})$ are the associated eigenvalues and eigenvectors. Solving this equation for the ground state with zero angular momentum simplifies this to putting the equation on a real space grid on r_{eh} , which yields the exciton binding energies reported in the main text.

Appendix C: Overlap density convergence

The bimolecular rate constant k_b is determined by the ratio of partition functions Z_c/Z_0 . The error from the path integral scales by the number of discretization factor as n^{-2} , so the convergence of the radiative rate can be extrapolated by fitting the ratios of partition functions at finite n as a function of n^{-2} . Extrapolations for CdS and MAPbI₃ are plotted in Fig. 8 (a) and (b) under different coupling strengths. Since the path integral formalism becomes exact in the limit of large number beads, the rate constant is defined as the value extrapolated to $1/n^2 \rightarrow 0$ limit.

REFERENCES

- ¹P. Umari, E. Mosconi, and F. De Angelis, “Infrared dielectric screening determines the low exciton binding energy of metal-halide perovskites,” *The journal of physical chemistry letters* **9**, 620–627 (2018).
- ²F. Thouin, A. R. Srimath Kandada, D. A. Valverde-Chávez, D. Cortecchia, I. Bargigia, A. Petrozza, X. Yang, E. R. Bitner, and C. Silva, “Electron–phonon couplings inherent in polarons drive exciton dynamics in two-dimensional metal-halide perovskites,” *Chemistry of Materials* **31**, 7085–7091 (2019).
- ³B. Miller, J. Lindlau, M. Bommert, A. Neumann, H. Yamaguchi, A. Holleitner, A. Högele, and U. Wurstbauer, “Tuning the fröhlich exciton-phonon scattering in monolayer mos₂,” *Nature communications* **10**, 1–6 (2019).
- ⁴E. Liu, J. van Baren, Z. Lu, T. Taniguchi, K. Watanabe, D. Smirnov, Y.-C. Chang, and C. H. Lui, “Exciton-polaron rydberg states in monolayer mose₂ and wse₂,” *Nature communications* **12**, 1–8 (2021).
- ⁵M. J. Schilcher, P. J. Robinson, D. J. Abramovitch, L. Z. Tan, A. M. Rappe, D. R. Reichman, and D. A. Egger, “The significance of polarons and dynamic disorder in halide perovskites,” *ACS Energy Letters* **6**, 2162–2173 (2021).
- ⁶W. Tao, Y. Zhang, and H. Zhu, “Dynamic exciton polaron in two-dimensional lead halide perovskites and implications for optoelectronic applications,” *Accounts of chemical research*, eabb7132 (2022).
- ⁷W. Tao, Q. Zhou, and H. Zhu, “Dynamic polaronic screening for anomalous exciton spin relaxation in two-dimensional lead halide perovskites,” *Science advances* **6**, eabb7132 (2020).
- ⁸H. Fröhlich, “Electrons in lattice fields,” *Advances in Physics* **3**, 325–361 (1954).
- ⁹T. D. Lee, F. E. Low, and D. Pines, “The Motion of Slow Electrons in a Polar Crystal,” *Physical Review* **90**, 297–302 (1953).
- ¹⁰T. Holstein, “Studies of polaron motion Part I. The molecular-crystal model,” *Annals of Physics* **8**, 325–342 (1959).
- ¹¹R. P. Feynman, “Mobility of Slow Electrons in a Polar Crystal,” *Physical Review* **127**, 1004–1017 (1962).
- ¹²C. Franchini, M. Reticioli, M. Setvin, and U. Diebold, “Polarons in materials,” *Nature Reviews Materials* **6**, 560–586 (2021).
- ¹³S. M. Ashok Chatterjee, *Polarons and Bipolarons* (CRC Press, 2019).

- ¹⁴K. Miyata, D. Meggiolaro, M. T. Trinh, P. P. Joshi, E. Mosconi, S. C. Jones, F. D. Angelis, and X.-Y. Zhu, “Large polarons in lead halide perovskites,” *Science Advances* **3**, e1701217 (2017).
- ¹⁵J. T. Devreese, “Fröhlich polarons. lecture course including detailed theoretical derivations,” (2015), arXiv:1012.4576 [cond-mat.other].
- ¹⁶M. Z. Mayers, L. Z. Tan, D. A. Egger, A. M. Rappe, and D. R. Reichman, “How lattice and charge fluctuations control carrier dynamics in halide perovskites,” *Nano Letters* **18**, 8041–8046 (2018).
- ¹⁷C. Wehrenfennig, G. E. Eperon, M. B. Johnston, H. J. Snaith, and L. M. Herz, “High Charge Carrier Mobilities and Lifetimes in Organolead Trihalide Perovskites,” *Advanced Materials* **26**, 1584–1589 (2014).
- ¹⁸S. D. Stranks, G. E. Eperon, G. Grancini, C. Menelaou, M. J. Alcocer, T. Leijtens, L. M. Herz, A. Petrozza, and H. J. Snaith, “Electron-hole diffusion lengths exceeding 1 micrometer in an organometal trihalide perovskite absorber,” *Science* **342**, 341–344 (2013).
- ¹⁹K. Cho, T. Yamada, H. Tahara, T. Tadano, H. Suzuura, M. Saruyama, R. Sato, T. Teranishi, and Y. Kanemitsu, “Luminescence Fine Structures in Single Lead Halide Perovskite Nanocrystals: Size Dependence of the Exciton-Phonon Coupling,” *Nano Letters* **21**, 7206–7212 (2021).
- ²⁰N. S. Ginsberg and W. A. Tisdale, “Spatially resolved photo-generated exciton and charge transport in emerging semiconductors,” *Annual review of physical chemistry* **71**, 1–30 (2020).
- ²¹L. Hedin, “New method for calculating the one-particle green’s function with application to the electron-gas problem,” *Physical Review* **139**, A796 (1965).
- ²²S. Albrecht, L. Reining, R. Del Sole, and G. Onida, “Excitonic effects in the optical properties,” *physica status solidi (a)* **170**, 189–197 (1998).
- ²³M. Rohlfing and S. G. Louie, “Electron-hole excitations and optical spectra from first principles,” *Physical Review B* **62**, 4927 (2000).
- ²⁴X. Wang and T. C. Berkelbach, “Excitons in solids from periodic equation-of-motion coupled-cluster theory,” *Journal of Chemical Theory and Computation* **16**, 3095–3103 (2020).
- ²⁵M. R. Filip and F. Giustino, “GW quasiparticle band gap of the hybrid organic-inorganic perovskite CH₃NH₃PbI₃: Effect of spin-orbit interaction, semicore electrons, and self-consistency,” *Physical Review B* **90**, 245145 (2014), 1410.2029.
- ²⁶B. D. Malone and M. L. Cohen, “Quasiparticle semiconductor band structures including spin-orbit interactions,” *Journal of Physics: Condensed Matter* **25**, 105503 (2013).
- ²⁷H. Haken, “Zur quantentheorie des mehrelektronensystems im schwingenden gitter. i,” *Zeitschrift für Physik* **146**, 527–554 (1956).
- ²⁸J. Pollmann and H. Büttner, “Effective hamiltonians and bindings energies of wannier excitons in polar semiconductors,” *Physical Review B* **16**, 4480 (1977).
- ²⁹J. Adamowski, B. Gerlach, and H. Leschke, “Treatment of the exciton-phonon interaction via functional integration. i. harmonic trial actions,” *Physical Review B* **23**, 2943 (1981).
- ³⁰M. R. Filip, J. B. Haber, and J. B. Neaton, “Phonon Screening of Excitons in Semiconductors: Halide Perovskites and Beyond,” *Physical Review Letters* **127**, 067401 (2021), 2106.08697.
- ³¹W. H. Sio, C. Verdi, S. Poncé, and F. Giustino, “Polarons from First Principles, without Supercells,” *Physical Review Letters* **122**, 246403 (2019), 1906.08402.
- ³²W. H. Sio, C. Verdi, S. Poncé, and F. Giustino, “Ab initio theory of polarons: Formalism and applications,” *Physical Review B* **99**, 235139 (2019), 1906.08408.
- ³³M. Schlipf, S. Poncé, and F. Giustino, “Carrier Lifetimes and Polaronic Mass Enhancement in the Hybrid Halide Perovskite CH₃NH₃PbI₃ from Multiphonon Fröhlich Coupling,” *Physical Review Letters* **121**, 086402 (2018), 1808.08130.
- ³⁴C. G. Bischak, C. L. Hetherington, H. Wu, S. Aloni, D. F. Ogle-tree, D. T. Limmer, and N. S. Ginsberg, “Origin of reversible photoinduced phase separation in hybrid perovskites,” *Nano letters* **17**, 1028–1033 (2017).
- ³⁵D. T. Limmer and N. S. Ginsberg, “Photoinduced phase separation in the lead halides is a polaronic effect,” *The Journal of Chemical Physics* **152**, 230901 (2020).
- ³⁶C. G. Bischak, A. B. Wong, E. Lin, D. T. Limmer, P. Yang, and N. S. Ginsberg, “Tunable polaron distortions control the extent of halide demixing in lead halide perovskites,” *The journal of physical chemistry letters* **9**, 3998–4005 (2018).
- ³⁷R. C. Remsing and J. E. Bates, “Effective mass path integral simulations of quasiparticles in condensed phases,” *The Journal of Chemical Physics* **153**, 121104 (2020), 2007.00599.
- ³⁸D. Chandler and K. Leung, “Excess electrons in liquids: Geometrical perspectives,” *Annual Review of Physical Chemistry* **45**, 557–591 (1994).
- ³⁹Y. Park, A. Obliger, and D. T. Limmer, “Nonlocal Screening Dictates the Radiative Lifetimes of Excitations in Lead Halide Perovskites,” *Nano Letters* **22**, 2398–2404 (2022).
- ⁴⁰J. Shumway and D. Ceperley, “Quantum monte carlo methods in the study of nanostructures,” *Quantum* **1**, 605 (2004).
- ⁴¹E. Mozafari, *Theoretical Description of the Electron-Lattice Interaction in Molecular and Magnetic Crystals* (Linköping LiU-Tryck, Linköping, Sweden, 2016).
- ⁴²R. P. Feynman, *Statistical Mechanics* (Westview, 1998).
- ⁴³R. P. Feynman and A. R. Hibbs, *Quantum Mechanics and Path Integrals* (Dover, 2005).
- ⁴⁴D. Chandler and P. G. Wolynes, “Exploiting the isomorphism between quantum theory and classical statistical mechanics of polyatomic fluids,” *The Journal of Chemical Physics* **74**, 4078–4095 (1981).
- ⁴⁵M. F. Herman, E. J. Bruskin, and B. J. Berne, “On path integral Monte Carlo simulations,” *The Journal of Chemical Physics* **76**, 5150–5155 (1982).
- ⁴⁶D. M. Ceperley, “Path integrals in the theory of condensed helium,” *Reviews of Modern Physics* **67**, 279 (1995).
- ⁴⁷L. E. Brus, “A simple model for the ionization potential, electron affinity, and aqueous redox potentials of small semiconductor crystallites,” *The Journal of Chemical Physics* **79**, 5566–5571 (1983).
- ⁴⁸Y. Cho and T. C. Berkelbach, “Optical properties of layered hybrid organic-inorganic halide perovskites: A tight-binding gw-bse study,” *The Journal of Physical Chemistry Letters* **10**, 6189–6196 (2019).
- ⁴⁹J. Contreras-Rascón, J. Díaz-Reyes, A. Flores-Pacheco, R. L. Morales, M. Álvarez Ramos, and J. Balderas-López, “Structural and optical modifications of CdS properties in CdS-Au thin films prepared by CBD,” *Results in Physics* **22**, 103914 (2021).
- ⁵⁰M. Sendner, P. K. Nayak, D. A. Egger, S. Beck, C. Müller, B. Epding, W. Kowalsky, L. Kronik, H. J. Snaith, A. Pucci, and R. Lovrinčić, “Optical phonons in methylammonium lead halide perovskites and implications for charge transport,” *Materials Horizons* **3**, 613–620 (2016), 1607.08541.
- ⁵¹L. Qiao, W. Fang, R. Long, and O. V. Prezhdo, “Extending Carrier Lifetimes in Lead Halide Perovskites with Alkali Metals by Passivating and Eliminating Halide Interstitial Defects,” *Angewandte Chemie* **132**, 4714–4720 (2020).

- ⁵²J. Schnitker and P. J. Rossky, “An electron–water pseudopotential for condensed phase simulation,” *The Journal of Chemical Physics* **86**, 3462–3470 (1987).
- ⁵³S. Plimpton, “Fast Parallel Algorithms for Short-Range Molecular Dynamics.” *J Comp Phys* **117**, 1–19 (1995).
- ⁵⁴J. T. Marshall and M. S. Chawla, “Feynman Path-Integral Calculation of the Polaron Effective Mass,” *Physical Review B* **2**, 4283–4287 (1970).
- ⁵⁵P. Kornilovitch, “Internal consistency of the path-integral calculation of the mass of the Fröhlich polaron,” *Physical Review B* **71**, 094301 (2005).
- ⁵⁶P. E. Kornilovitch, “Continuous-Time Quantum Monte Carlo Algorithm for the Lattice Polaron,” *Physical Review Letters* **81**, 5382–5385 (1998).
- ⁵⁷D. Scharf, J. Jortner, and U. Landman, “Atomic and molecular quantum mechanics by the path integral molecular dynamics method,” *Chemical Physics Letters* **130**, 504–510 (1986).
- ⁵⁸P. Y. Yu and M. Cardona, *Fundamentals of Semiconductor: Physics and Materials properties* (Springer, New York, 2010).
- ⁵⁹M. Baranowski and P. Plochocka, “Excitons in Metal-Halide Perovskites,” *Advanced Energy Materials* **10**, 1903659 (2020).
- ⁶⁰Y. Toyozawa, M. Ueta, H. Kanzaki, K. Kobayashi, and E. Hanamura, “Excitonic processes in solids,” *Springer Series in Solid-State Sciences* **60**, 203 (1986).
- ⁶¹L. M. Herz, “Charge-carrier dynamics in organic-inorganic metal halide perovskites,” *Annual Review of Physical Chemistry* **67**, 65–89 (2016).
- ⁶²M. B. Johnston and L. M. Herz, “Hybrid Perovskites for Photovoltaics: Charge-Carrier Recombination, Diffusion, and Radiative Efficiencies,” *Accounts of Chemical Research* **49**, 146–154 (2016).
- ⁶³J. P. Philbin and E. Rabani, “Electron–hole correlations govern auger recombination in nanostructures,” *Nano Letters* **18**, 7889–7895 (2018).
- ⁶⁴J. P. Philbin, A. Brumberg, B. T. Diroll, W. Cho, D. V. Talapin, R. D. Schaller, and E. Rabani, “Area and thickness dependence of auger recombination in nanoplatelets,” *The Journal of Chemical Physics* **153**, 054104 (2020).
- ⁶⁵M. Wimmer, S. V. Nair, and J. Shumway, “Biexciton recombination rates in self-assembled quantum dots,” *Physical Review B* **73** (2006), 10.1103/physrevb.73.165305, cond-mat/0512603.
- ⁶⁶J. M. Frost, “Calculating polaron mobility in halide perovskites,” *Physical Review B* **96**, 195202 (2017), 1704.05404.
- ⁶⁷A. Veamatahau, B. Jiang, T. Seifert, S. Makuta, K. Latham, M. Kanehara, T. Teranishi, and Y. Tachibana, “Origin of surface trap states in CdS quantum dots: relationship between size dependent photoluminescence and sulfur vacancy trap states,” *Physical Chemistry Chemical Physics* **17**, 2850–2858 (2014).
- ⁶⁸D. Meggiolaro, S. G. Motti, E. Mosconi, A. J. Barker, J. Ball, C. A. R. Perini, F. Deschler, A. Petrozza, and F. D. Angelis, “Iodine chemistry determines the defect tolerance of lead-halide perovskites,” *Energy & Environmental Science* **11**, 702–713 (2018).
- ⁶⁹M. R. Shirts and J. D. Chodera, “Statistically optimal analysis of samples from multiple equilibrium states,” *The Journal of Chemical Physics* **129**, 124105 (2008), 0801.1426.
- ⁷⁰D. B. R. H. S. S. Kumar, J. M. Rosenberg and P. A. Kollman, “THE weighted histogram analysis method for free-energy calculations on biomolecules. I. The method,” *Journal of Computational Chemistry* **13**, 1011 (1992).
- ⁷¹A. Grossfield, “WHAM: the weighted histogram analysis method, version 2.0.10.2,” http://membrane.urmc.rochester.edu/wordpress/?page_id=126.